Sustainable Energy & Fuels

ROYAL SOCIETY OF CHEMISTRY

PAPER

View Article Online
View Journal | View Issue

Check for updates

Cite this: *Sustainable Energy Fuels*, 2026, **10**, 1348

Formation of mixed-phase $Ni_xB/Co_3O_4/Co(OH)_2$ and its application as a pre-catalyst for the oxygen evolution reaction

Gillian Collins,[a] Ramaraj Sukanya,[a] Daniele Alves,[a] Thamaraiselvi Kanagaraj,[b] Raj Karthik,[a] Tara N. Barwa,[a] Jae-Jin Shim[b] and Carmel B. Breslin*[ac]

Herein, a mixed-phase nickel boride/cobalt oxide/cobalt hydroxide, $Ni_xB/Co_3O_4/Co(OH)_2$, composite was formed to give a scalable and non-precious pre-catalyst for the oxygen evolution reaction (OER) in alkaline medium. The material was synthesised *via* a simple chemical reduction method, where amorphous Ni_xB particles were deposited onto cobalt oxide rods undergoing partial transformation into $Co(OH)_2$ sheets. This approach suppresses the agglomeration of Ni_xB particles, increasing surface accessibility. The optimised composite (Ni_xB/Co_3O_4-100 mg/$Co(OH)_2$) achieved a low overpotential of 370 mV at 100 mA cm^{-2}. It retained 99.2% of its activity after more than 90-h of continuous operation at 100 mA cm^{-2} for the OER in 1.0 M KOH, indicating excellent stability. Electrochemical impedance analysis revealed a 20-fold increase in the electroactive surface area compared to the bare substrate. XPS analysis following stability testing under OER conditions confirmed a full surface reconstruction, with the loss of boron from the surface and formation of catalytically active NiOOH and CoOOH species, indicating that Ni_xB, Co_3O_4 and $Co(OH)_2$ act as precursors to the true active phase. This work highlights a practical strategy for designing robust, non-precious OER catalysts through the phase reconstruction of boride/oxide hybrids.

Received 13th November 2025
Accepted 5th February 2026

DOI: 10.1039/d5se01506e

rsc.li/sustainable-energy

Open Access Article. Published on 05 February 2026. Downloaded on 4/16/2026 1:51:50 AM.
This article is licensed under a Creative Commons Attribution 3.0 Unported Licence.

1. Introduction

Hydrogen production *via* water electrolysis is a promising option for sustainable energy, but its efficiency is limited by the oxygen evolution reaction (OER) half-reaction, which is a complex, four-electron process that demands a substantial energy input.[1] As the rate-limiting step, OER directly influences the energy requirement and cost of hydrogen production, necessitating the development of high-performing, non-precious OER catalysts critical to lowering the overall energy requirements for water-splitting applications.[2] Conventional OER catalysts, such as iridium and ruthenium oxides, deliver high performance but are costly and limited in supply, necessitating the exploration of new materials with comparable catalytic efficacy.[3,4]

Transition metal (TM)-based compounds, particularly pre-catalysts that undergo *in situ* surface reconstruction to form active (oxy)hydroxide layers under OER conditions, have emerged as viable electrocatalysts due to their enhanced active-site density and stability.[5–8] This surface transformation process is associated with improved catalytic performance. Indeed, numerous studies report that the *in situ* oxidation of chalcogenides results in significantly higher surface areas than their TM-oxide equivalents, through surface transformation, enhancing the OER activity.[5,8–10]

Among these, transition metal borides (TMBs) have gained attention as a promising class of materials for catalytic applications due to their structural versatility, electronic characteristics, and high specific capacity.[11,12] The performance of Ni_xB is rooted in its electron-rich nickel centres, created by partial electron transfer from boron to nickel.[13] This electronic redistribution lowers kinetic barriers, facilitating charge transfer and enhancing the binding of reaction intermediates. In its amorphous form, Ni_xB benefits from a disordered structure that offers a high density of exposed active sites, particularly favourable for OH^- adsorption, a key step in efficient water oxidation. The morphology of Ni_xB nanoparticles further enhances these properties by maximising surface area and promoting rapid electron and ion transport, which are essential qualities for OER catalysis.[14] In addition, Ni_xB can transform into highly active NiOOH species through surface reconstruction, thereby exposing electron-rich Ni sites optimal for the conversion of OER intermediates.[15] Despite these advantages, Ni_xB particles tend to aggregate, reducing the accessibility of their active sites. Previous studies have explored strategies to improve Ni_xB dispersion and performance by anchoring it to

[a]*Department of Chemistry, Maynooth University, Maynooth, Co. Kildare, Ireland. E-mail: Carmel.Breslin@mu.ie*

[b]*School of Chemical Engineering, Yeungnam University, 280 Daehak-ro, Gyeongsan, Gyeongbuk 38541, Republic of Korea*

[c]*Kathleen Lonsdale Institute, Maynooth University, Maynooth, Co. Kildare, Ireland*

This journal is © The Royal Society of Chemistry 2026

Open Access Article. Published on 05 February 2026. Downloaded on 4/16/2026 1:51:50 AM. This article is licensed under a Creative Commons Attribution 3.0 Unported Licence.

various supports.[16–19] However, many of these supports are either catalytically inert, unstable under OER conditions or rely on platinum group metals (PGMs), which limit practicality for sustainable water-splitting systems.[20]

On the other hand, cobalt oxides such as Co_3O_4 and $Co(OH)_2$, which similarly convert to CoOOH under anodic bias,[20] offer complementary redox properties, high conductivity, and morphological tunability, making them ideal as supports for hybrid Ni_xB/Co-based composites. Moreover, these cobalt oxides can be readily tailored into rod- and sheet-like morphologies, increasing the exposed surface area and improving contact between active sites and the electrolyte.[21,22] Co_3O_4, a mixed-valence state and spinel-type oxide, offers high conductivity and multiple accessible oxidation states, while $Co(OH)_2$ serves as a common *in situ* precursor to active oxyhydroxide species under OER conditions. These properties make them suitable as catalytically relevant supports for anchoring amorphous Ni_xB, which are otherwise prone to aggregation. The combination of a cobalt-based support with Ni_xB may therefore address the dual challenge of aggregation and catalytic stability and performance, whilst avoiding the limitations of unsuitable or PGM support systems.

In this work, we present a simple, scalable chemical reduction strategy to prepare a mixed-phase $Ni_xB/Co_3O_4/Co(OH)_2$ composite as a pre-catalyst for alkaline OER. *In situ* reduction of Ni^{2+} and partial transformation of Co_3O_4 rods into $Co(OH)_2$ sheets yield a hybrid structure that supports active site exposure, while suppressing Ni_xB agglomeration. Under anodic bias, the material undergoes surface reconstruction, forming the catalytically active nickel and cobalt (oxy)hydroxide species. Aiming to evaluate the true intrinsic behaviour of the $Ni_xB/Co_3O_4/Co(OH)_2$ catalyst without substrate interference, carbon cloth (CC) was used for the initial screening because it is largely inactive towards the OER. Therefore, it provides a cleaner baseline for comparing catalyst formulations without a strong substrate contribution, allowing the electrochemical response to be assigned primarily to the deposited catalyst rather than the substrate. This is particularly important for metrics such as electrochemical surface area (ECSA), Tafel slopes, CV redox features, and LSV-derived overpotentials, which can be distorted as an active current collector can also contribute to faradaic processes. However, carbon-based materials, including CC, are not ideal for extended anodic operation in alkaline media as carbon is prone to oxidative degradation under prolonged anodic conditions, which limits their suitability for durability studies.[23] Therefore, following initial screening, the optimised composite was transferred onto a nickel foam (NF) substrate, which offers high electrical conductivity, a 3D porous architecture that improves electrolyte access and bubble release, and mechanical robustness under alkaline electrolysis conditions. The resulting material achieves an overpotential of 370 mV at 100 mA cm^{-2} with stability maintained over a 90-h period. Post-analysis XPS confirms complete surface reconstruction to catalytically active NiOOH and CoOOH, indicating that $Ni_xB/Co_3O_4/Co(OH)_2$ acts as a precursor for this active catalyst.

While Ni_xB particles and Co_3O_4 have been used as electrocatalysts, this unique combination of $Ni_xB/Co_3O_4/Co(OH)_2$ has not, to the best of our knowledge, been previously utilised as a pre-catalyst for the OER. This makes it an interesting material, where the Co_3O_4 rods are partially converted to $Co(OH)_2$ sheets, which can then readily form the active CoOOH surface phase, while the Ni_xB serves as a source of NiOOH. This work contributes to the growing body of research on boride-based pre-catalysts, offering practical insights into hybrid support design, transformation-driven catalysis, and long-term OER stability in alkaline conditions.

2. Experimental

Detailed information about the materials, reagents, material characterisation, and electrochemical measurements on the prepared materials can be found in the SI.

2.1 Synthesis of Co_3O_4 rods

In separate beakers, 1.19 g of $CoCl_2$ (A1), 1.5 g of urea (B1), and 0.05 g of CTAB (cetyltrimethylammonium bromide) (C1) were each dissolved in 10 mL of deionised water (DI water) under stirring at 700 rpm, forming solutions A1, B1, and C1, respectively. After 10 min of mixing, solutions B1 and C1 were combined into solution A1 very slowly to ensure homogeneity. The combined mixture was then transferred to a Teflon-lined autoclave and heated at 120 °C for 12 h. After the reaction, the resulting product was washed thoroughly with deionised (DI) water and ethanol. The material was dried overnight at 50 °C. Finally, the dried product was calcined at 300 °C for 2 h. After calcination, the material was allowed to cool to room temperature and stored for further use. This methodology is illustrated in Scheme 1(a).

2.2 Synthesis of amorphous nickel boride (Ni_xB)

0.742 g of $NiCl_2$ was transferred to a beaker containing 25 mL of DI water and stirred at 700 rpm for 10 min, and labelled as solution A2. Separately, 0.189 g of $NaBH_4$, a reducing agent and source of boron, was dissolved in 10 mL of DI water with 0.02 g of NaOH, and the mixture was labelled as solution B2. After 10 min, solution A2 was transferred to an ice-bath set up to maintain the reaction temperature at 0 °C. After 20 min of continuous stirring under a N_2 atmosphere, solution B2 was slowly added dropwise to solution A2 using a syringe. Upon the addition of solution B2, an effervescence began, and a black precipitate formed immediately. The reaction was carried out for 30 min under an N_2 atmosphere and stirring at 700 rpm at 0 °C. After the reaction, the precipitate was washed thoroughly with DI water and finally with ethanol. The powder was dried overnight at 50 °C and stored for further use.

2.3 Preparation of $Ni_xB/Co_3O_4/Co(OH)_2$

The $Ni_xB/Co_3O_4/Co(OH)_2$ composites were synthesised *via* an *in situ* chemical reduction process, as shown in Scheme 1(b) and (c). Pre-synthesised Co_3O_4 (50, 100, or 150 mg) was dispersed in 25 mL of DI water and sonicated for 10 min to ensure uniform dispersion. These suspensions were transferred to a Buchner flask and stirred at 700 rpm, designated as solution A3. Separately, 0.742 g of $NiCl_2$ was weighed out, and the nickel salt was

Open Access Article. Published on 05 February 2026. Downloaded on 4/16/2026 1:51:50 AM.
This article is licensed under a Creative Commons Attribution 3.0 Unported Licence.

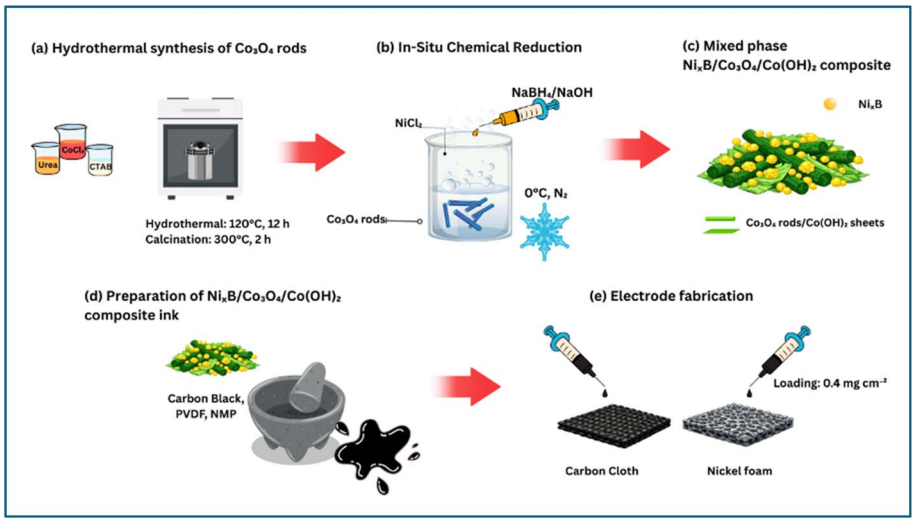

Scheme 1 Schematic representation of the preparation and fabrication of the electrocatalysts on CC and NF.

slowly added to solution A3, which was then stirred for an additional 10 min to give solution B3. After 10 min, this solution was transferred to an ice-bath and maintained at 0 °C. Separately, 0.189 g of $NaBH_4$ in 10 mL DI water with 0.02 g NaOH was prepared and labelled as solution C3. After 20 min of continuous stirring under a N_2 atmosphere, solution B3 was slowly added dropwise to the Co_3O_4/Ni mixture (solution C3) using a syringe. The reaction proceeded under these conditions for an additional 30 min, with a gradual formation of $Co(OH)_2$ sheets alongside the Co_3O_4 rods due to the basic and reducing atmosphere. The final composite materials, consisting of Co_3O_4 rods and $Co(OH)_2$ sheets and amorphous Ni_xB, were washed thoroughly with DI water and ethanol, dried overnight at 50 °C and stored for further analysis. Samples were designated as Ni_xB/CoO-50, as Ni_xB/CoO-100, and as Ni_xB/CoO-150, corresponding to the initial Co_3O_4 rod mass used.

2.4 Electrode preparation and coating

Carbon cloth (CC) electrodes were prepared by cutting a 1 × 2 cm^2 piece of commercial CC. The CC was cleaned *via* 5-min sonication in 1.0 M HCl and washed with DI water and ethanol, followed by overnight drying at 60 °C. The catalyst slurry ink was then prepared by mixing 81% of the active material, 14% carbon black, and 5% polyvinylidene fluoride (PVDF) as a binder, with sufficient *N*-methyl-2-pyrrolidone (NMP) as a solvent. Finally, the slurry was evenly coated onto the CC in a 1 × 1 cm^2 area of the CC substrate and dried at 50 °C between the layers, resulting in a final catalyst loading of 0.4 mg cm^{-2}, as illustrated in Scheme 1(d) and (e). This was found to be the optimal loading. The influence of Ni_xB/CoO-100 loadings is summarised in Table S1. While loadings between 0.1 and 0.6 mg cm^{-2} have little influence at lower overpotentials, the 0.4 mg cm^{-2} loading exhibits the lowest overpotential during the OER at a current density of 50 mA cm^{-2}.

Nickel foam (NF) electrodes were prepared by cutting a 1 × 1 cm^2 piece of commercial NF. NF can be difficult to standardise due to its disordered porosity and variability between samples, leading to a wide range of baseline performances reported in the literature.[24] To minimise variability and improve reproducibility, 1 × 1 cm^2 NF pieces were pre-weighed and matched in mass across experiments. Each was connected to a nickel wire (all of equal weight), cleaned with acetone, and then electrochemically reduced by immersing the NF in 1.0 M KOH at −1.0 V (*vs.* Hg/HgO) for 10 min to remove surface oxides. It was then pressed to a uniform thickness of approximately 0.1 mm to provide a planar surface, facilitating the coating process. The slurry was prepared as above, but without the addition of conducting carbon black, as NF is intrinsically conducting. Like the CC, a final catalyst loading of 0.4 mg cm^{-2} was maintained.

3. Results and discussion

3.1 Characterisation of materials

The composite was prepared *via* an *in situ* chemical reduction process, in which amorphous Ni_xB particles were deposited onto a cobalt-based support undergoing partial phase transformation. Specifically, the as-prepared Co_3O_4 rods were exposed to the highly alkaline and reducing environment generated by $NaBH_4$ and NaOH. Under these conditions, Co^{3+} ions within the Co_3O_4 lattice are partially reduced to Co^{2+}, and this, along with the existing Co^{2+} in the oxide phase, promotes the formation of $Co(OH)_2$ sheets. Simultaneously, Ni^{2+} is reduced to form amorphous Ni_xB, which nucleates and deposits across the $Co_3O_4/Co(OH)_2$ surface. The result is a multidimensional composite comprising Ni_xB particles interfacing with $Co(OH)_2$ sheets as well as Co_3O_4 rods. The reaction pathway can be summarised in eqn (1) and (2).

$$Co_3O_4 + 3H_2O \rightarrow 3Co(OH)_2 + \tfrac{1}{2}O_2 \quad (1)$$

$$Ni^{2+} + 2BH_4^- + 3H_2O \rightarrow Ni_xB + B(OH)_3 + 5\tfrac{1}{2}H_2 \quad (2)$$

The morphology and structural transformation within the $Ni_xB/Co_3O_4/Co(OH)_2$ composite were initially examined through field-emission scanning electron microscopy (FE-SEM),

 This journal is © The Royal Society of Chemistry 2026

Open Access Article. Published on 05 February 2026. Downloaded on 4/16/2026 1:51:50 AM.
This article is licensed under a Creative Commons Attribution 3.0 Unported Licence.

as shown in Fig. 1. FE-SEM images of pristine Co_3O_4 rods (Fig. 1(a)) display well-defined rod-like structures with varying lengths. These rod-like features are more readily seen in the inset in Fig. 1(a) and provide a favourable morphology for maximising surface area and enhancing electron transport, critical factors for electrochemical applications. In contrast, the amorphous Ni_xB phase, prepared without the addition of the Co_3O_4 rods (Fig. 1(b) and the inset in Fig. 1(b)), is observed as spherical aggregated particles. FE-SEM analysis of the final composite (Fig. 1(c) and (d)) reveals a more complex architecture, where both Co_3O_4 rods and newly formed 2D sheet-like $Co(OH)_2$ structures coexist, decorated with dispersed spherical Ni_xB particles. This transformation from rods to sheets is likely promoted by the introduction of $NaBH_4$ during the decoration process, resulting in a mixed-phase $Co_3O_4/Co(OH)_2$ support that helps reduce Ni_xB agglomeration and improve electrochemical accessibility. Energy-dispersive X-ray (EDX) mapping (Fig. 1(e–h)) further confirms the uniform distribution of Co, Ni, O, and B elements across the composite, indicating successful integration of Ni_xB with Co_3O_4 and $Co(OH)_2$.

X-ray diffraction (XRD) analysis was performed to confirm the incorporation of amorphous Ni_xB and to investigate phase transformations within the Co_3O_4 rods during Ni_xB deposition. As shown in Fig. 2(b), the XRD pattern of pristine Co_3O_4 exhibits

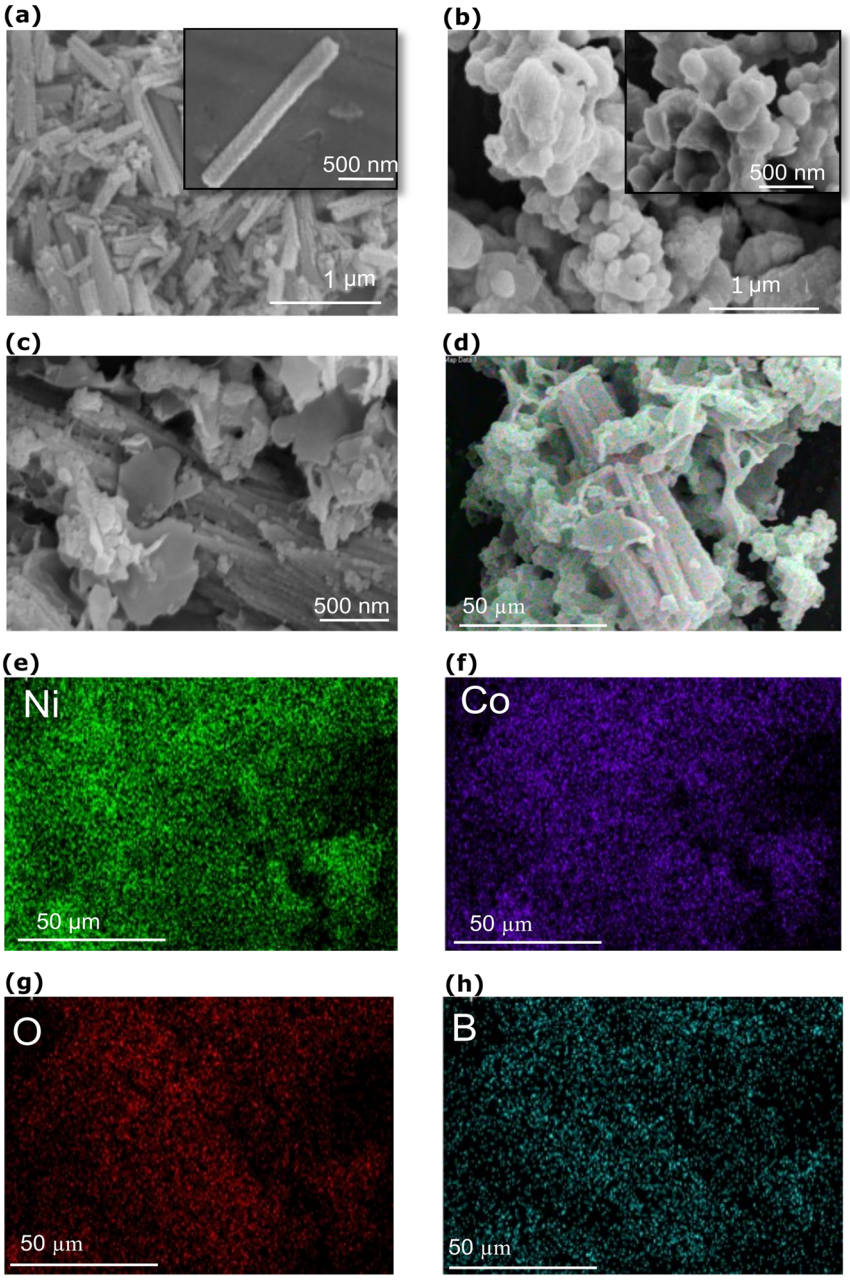

Fig. 1 FE-SEM micrographs of (a) hydrothermally prepared Co_3O_4 rods, (b) Ni_xB and (c and d) as-prepared $Ni_xB/Co_3O_4/Co(OH)_2$ (with 100 mg of Co_3O_4) composite and (e–h) EDX elemental mapping, highlighting the distributions of Ni, Co, O and B in the composite.

Open Access Article. Published on 05 February 2026. Downloaded on 4/16/2026 1:51:50 AM.
This article is licensed under a Creative Commons Attribution 3.0 Unported Licence.

sharp peaks at 19.0°, 31.3°, 36.8°, 38.5°, 44.8°, 59.3°, and 65.2°, corresponding to the (111), (220), (222), (311), (400), (511), and (440) planes of cubic Co_3O_4 (JCPDS 00-001-1152). In contrast, pristine Ni_xB displays a broad, undefined peak between 40° and 50°, characteristic of its amorphous nature.[25] In the composite samples, the XRD patterns display sharp reflections indicative of crystalline Co_3O_4, along with a broad feature associated with amorphous Ni_xB. The broad amorphous Ni_xB peak around 45° is more prominent in the sample with the highest Ni_xB to Co_3O_4 ratio (CoONiB-50), but it is present in all composites, confirming successful integration of amorphous Ni_xB into the Co_3O_4/$Co(OH)_2$ support. Additionally, a broad peak appears in the 2θ range of 10–20°, consistent with the formation of a $Co(OH)_2$ phase.[26] This is attributed to the reducing and alkaline conditions generated during the chemical reduction process. Notably, the intensity of this broad peak increases with higher initial Co_3O_4 content, suggesting that the composites with a higher Co_3O_4 to Ni_xB ratio exhibit a greater extent of $Co(OH)_2$ sheet formation.

Further evidence of cobalt phase transformation was obtained through Fourier-transform infrared (FTIR) spectroscopy (Fig. 2(a)). In pristine Co_3O_4, peaks corresponding to Co–O stretching vibrations are observed in the 560–660 cm^{-1} region, consistent with previous reports.[27,28] In the composite, these peaks diminish and broaden, reflecting disruption in the lattice structure and supporting the formation of $Co(OH)_2$.[26] Additionally, a new peak observed at 972 cm^{-1} in the composites can be assigned to O–H deformation vibrations of $Co(OH)_2$.[29]

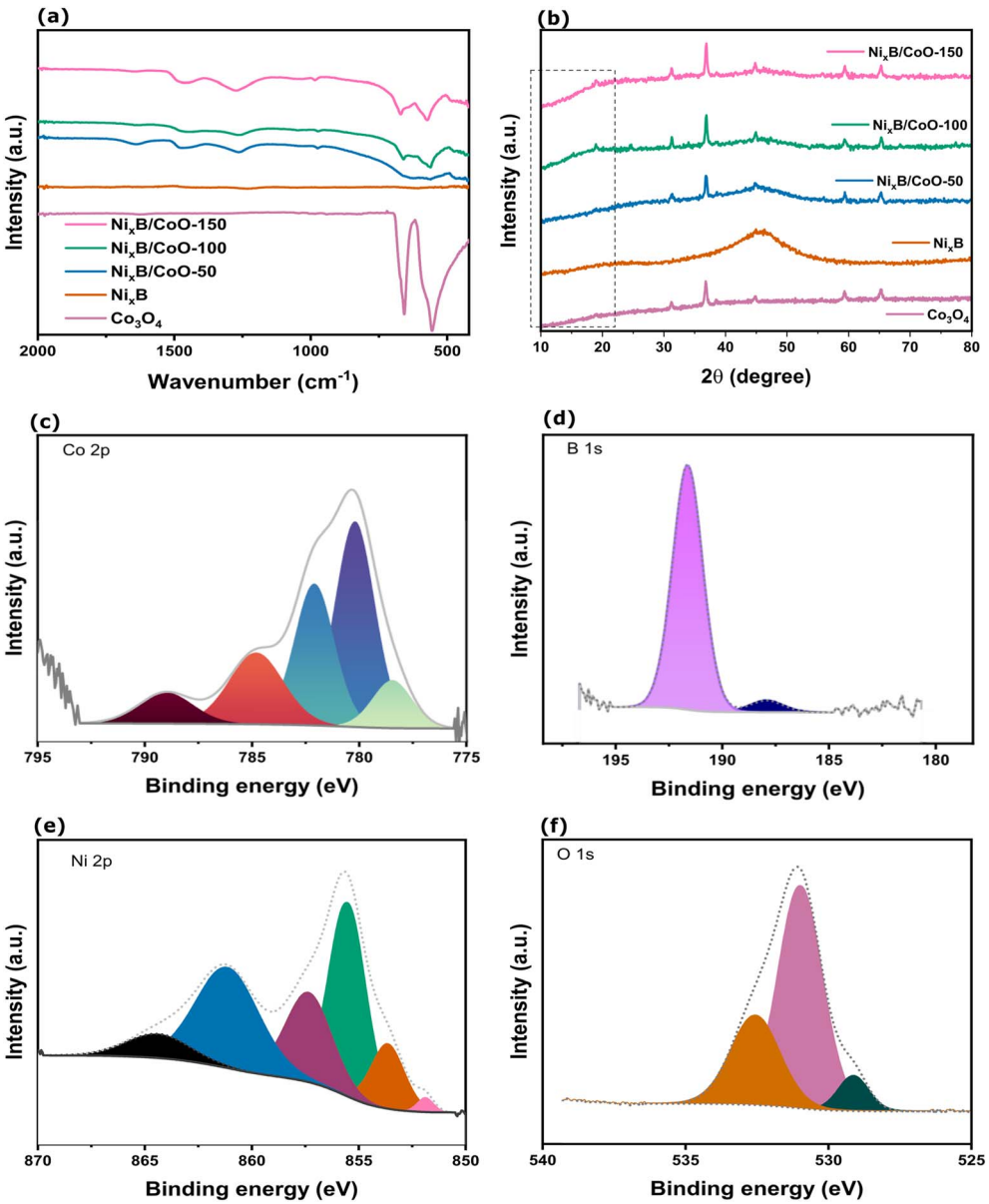

Fig. 2 (a) FTIR spectrum and (b) XRD pattern of Ni_xB/CoO composite, and XPS spectra of (c) Co 2p, (d) B 1s, (e) Ni 2p, and (f) O 1s of the Ni_xB/CoO-100 composite.

This journal is © The Royal Society of Chemistry 2026

Open Access Article. Published on 05 February 2026. Downloaded on 4/16/2026 1:51:50 AM.
This article is licensed under a Creative Commons Attribution 3.0 Unported Licence.

Collectively, these analyses indicate that the composites undergo a significant partial phase transformation, resulting in a unique structure consisting of Co_3O_4 rods, partially converted into $Co(OH)_2$ sheets, with amorphous Ni_xB particles distributed throughout the cobalt-based support. The incorporation of amorphous Ni_xB, known for its distinct electronic properties, contributes an additional catalytic component to the material, thereby enhancing its electrochemical performance. This mixed-phase structure increases the available surface area and active site density, enabling contributions from each component during electrochemical operation.

The elemental composition and electronic states of the Ni_xB/CoO-100 composite material were investigated through X-ray photoelectron spectroscopy (XPS). The survey spectrum is shown in Fig. S1, confirming the presence of Co, Ni, O and B elements in the composite. As shown in Fig. 2, the high-resolution analysis of the Co 2p spectra (Fig. 2(c)) reveals two major peaks at binding energies of 780.2 and 782.1 eV, which are dominated by multiplet splitting and satellite features typical of mixed cobalt oxide/hydroxide systems, consistent with the presence of Co_3O_4 and $Co(OH)_2$.[30] Additionally, a peak appears at 778.5 eV, which may be attributed to the metallic cobalt.[31] The B 1s region (Fig. 2(d)) exhibits two peaks at 187.9 and 191.6 eV, corresponding to Ni–B and B–O bonds, respectively. These binding energy values align well with those reported in the literature for nickel boride-based heterostructures.[14] The Ni 2p spectrum (Fig. 2(e)) was deconvoluted into three peaks located at 851.9, 853.6 and 855.5 eV,

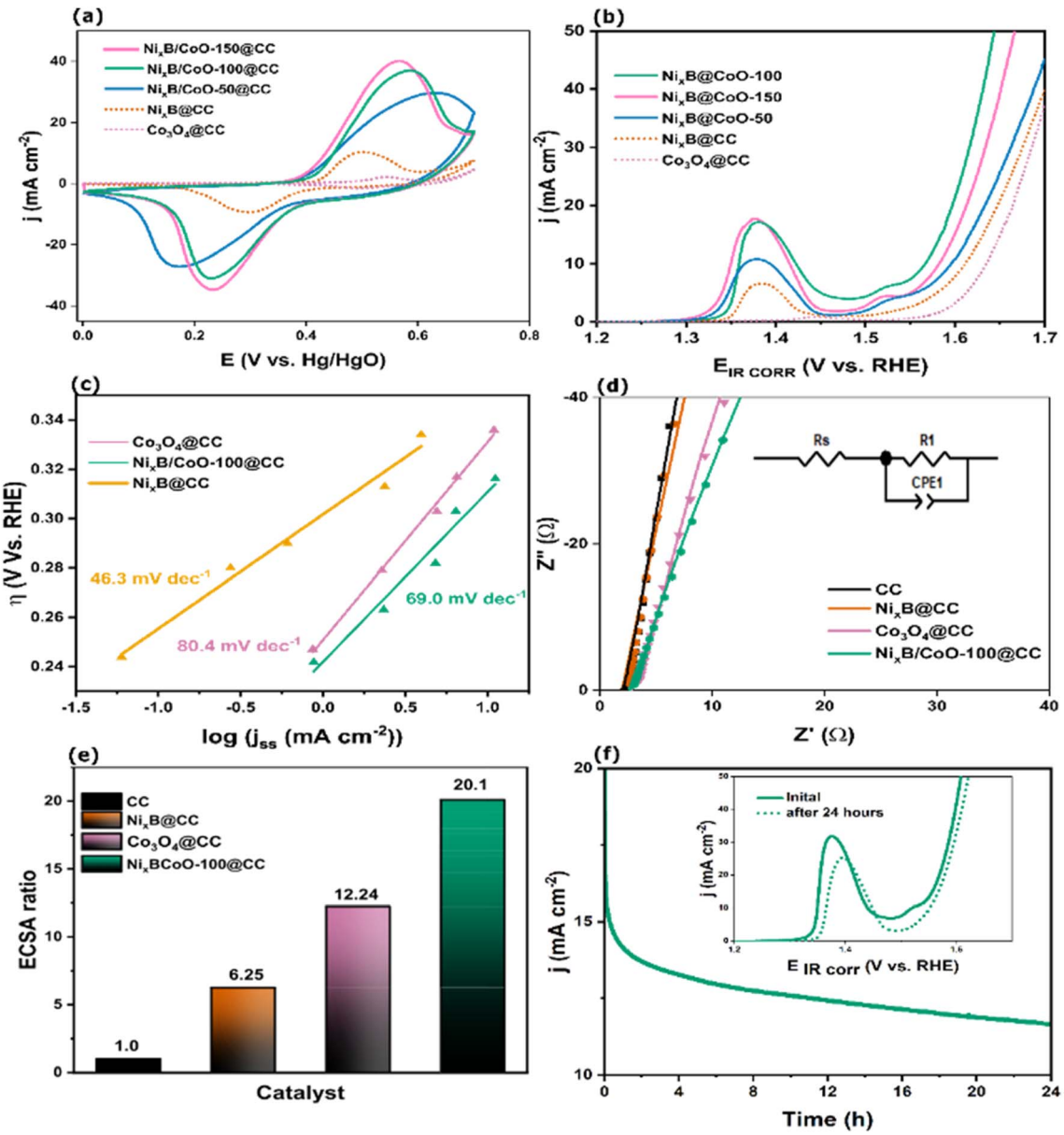

Fig. 3 Electrochemical characterisation of composite materials on CC substrate in 1.0 M KOH: (a) CV cycling at 50 mV s^{-1} (b) IR-corrected LSV at 2 mV s^{-1}, (c) Tafel slopes comparing OER kinetics, (d) EIS of non-faradic region, (e) ECSA ratio compared to bare substrate, (f) chronoamperometry of Ni_xB/CoO-100@CC over 24 h with inset showing post-24-h LSV.

Open Access Article. Published on 05 February 2026. Downloaded on 4/16/2026 1:51:50 AM. This article is licensed under a Creative Commons Attribution 3.0 Unported Licence.

which are assigned to Ni–B and Ni–O and $Ni(OH)_2$ species, respectively.[32] The O 1s (Fig. 2(f)) spectrum displays two distinct peaks at 529.1 and 531.0 eV corresponding with metal-oxide and metal hydroxide bonding, respectively.

3.2 Electrochemical performance of Ni_xB/CoO on CC

The electrochemical performances of the Ni_xB/CoO composites (Ni_xB/CoO-50, Ni_xB/CoO-100, Ni_xB/CoO-150) were screened for the OER on the catalytically inert CC substrate in 1.0 M KOH. Prior to catalytic testing, each electrode was electrochemically activated by cyclic voltammetry (CV) between 0.0 V and 0.7 V (*vs.* Hg/HgO) at a scan rate of 50 mV s^{-1} in 1.0 M KOH until a stable state was achieved. This activation has previously been shown to be an effective strategy to improve the OER performance of transition metals.[33] A stable state was reached after approximately 10 cycles, as illustrated in supplementary data, Fig. S2. Comparative CV curves for each composite are shown in Fig. 3(a) following 10 cycles. The composites exhibit higher anodic and cathodic peak currents relative to the control samples (Ni_xB and Co_3O_4), suggesting improved electrochemical activity compared to the individual components. This enhancement may be due to increased surface area and more accessible redox sites provided by the composite structure. The CV recorded for Co_3O_4 reveals only a minor oxidation wave, associated with the oxidation of the metallic Co observed in the XPS, to Co^{2+}, with no indication of the reverse reaction. Hence, the more prominent redox peaks in Fig. 3(a) signify the interconversion between Ni^{2+} and Ni^{3+} with quasi-reversible behaviour. Notably, the peak-to-peak separation varies with the amount of Co_3O_4 added, exhibiting the smallest separation and sharper peaks for Ni_xB/CoO-100@CC. This indicates that this particular composite demonstrates superior electrical conductivity.

Following activation, linear sweep voltammetry (LSV) was performed at 2 mV s^{-1} in 1.0 M KOH and cycled from 0.0 V to 1.5 V *vs.* Hg/HgO. These data were subjected to IR correction using an 85% correction. The impact of this correction is illustrated in Fig. S3, where the IR-corrected and non-corrected plots are compared. As expected, the IR correction has a greater influence at higher currents. In Fig. 3(b), the LSV plots are displayed for the different composites, while the LSV plots for CC and the benchmark RuO_2 are provided in Fig. S4. Among the composites prepared with varying Co_3O_4 content, Ni_xB/CoO-100@CC exhibited the highest OER activity with an overpotential of 410 mV at a current density of 50 mA cm^{-2} on CC compared to the values of 435, 478, 492 and 495 mV for Ni_xB/CoO-150@CC, Ni_xB/CoO-50@CC, Co_3O_4@CC and Ni_xB@CC, respectively. In the LSV plots in Fig. 3(b), two redox events are also clearly evident. The peak centred at 1.38 to 1.40 V (*vs.* RHE) is consistent with the Ni^{2+}/Ni^{3+} conversion. However, the conversion of Co_3O_4 to CoOOH, eqn (3), which has a standard reduction potential of 1.22 V *vs.* RHE,[34] may also contribute to this peak. Indeed, this conversion is evident in the absence of nickel with the Co_3O_4@CC, where the oxidation wave is centred at 1.45 V. With the good conductivity of the Ni_xB/CoO-100@CC composites, this reduction may be more thermodynamically favourable, shifting to a somewhat lower potential to coincide with the Ni^{2+}/Ni^{3+} conversion. Interestingly, the shoulder peak observed for all the Ni_xB/CoO composites may indicate the transformation of the $Co(OH)_2$ sheets into CoOOH, eqn (4). This conversion has been observed at 1.58 V,[35] which is in good agreement with the position of this shoulder peak in Fig. 3(b) at 1.52 V.

$$Co_3O_4 + OH^- + H_2O \leftrightharpoons 3CoOOH + e^- \quad (3)$$

$$Co(OH)_2 + OH^- \leftrightharpoons CoOOH + H_2O + e^- \quad (4)$$

Clearly, the Ni_xB/CoO-100@CC exhibits the highest OER activity, particularly at higher overpotentials, and was therefore selected for the OER studies and compared with its individual components, Co_3O_4@CC and Ni_xB@CC.

To investigate OER kinetics, Tafel slope analysis was performed on Ni_xB/CoO-100@CC. Notably, an oxidation peak linked to the formation of NiOOH, which obscures the Tafel region, was observed in the LSV curves (Fig. 3(b)), which complicates the determination of the true Tafel slope. Therefore, the Tafel plots were constructed from steady-state measurements rather than potentiodynamic data, which often suffer from non-steady-state effects, double-layer charging, and self-oxidation artefacts.[36] The steady-state current densities (j_{ss}) were obtained by chronoamperometry at various overpotentials in the Tafel region (Fig. S5). The Ni_xB/CoO-100@CC composite exhibited a Tafel slope of 69.0 mV dec^{-1}, while Ni_xB@CC and Co_3O_4@CC gave slopes of 46.3 and 80.4 mV dec^{-1} (Fig. 3(c)), respectively. It is well established that the apparent Tafel slope can shift with potential, surface coverage, and catalyst loading.[37] These values were therefore used for comparison of the components of the Ni_xB/CoO-100@CC composite, rather than a mechanistic analysis. Within this region, Ni_xB@CC exhibits the lowest slope, meaning the current increases more rapidly per unit increase in overpotential, indicating simpler reaction dynamics with faster electron transfer and fewer intermediate transitions. However, as a single-phase material, Ni_xB@CC does not benefit from the added active site diversity seen in the mixed-phase Ni_xB/CoO-100@CC composite. The Co_3O_4@CC reference catalyst exhibited a Tafel slope of 98.4 mV dec^{-1}, indicating moderate electron transfer efficiency without the additional catalytic effects provided by the composite structure. Overall, the Ni_xB/CoO-100@CC composite demonstrated lower overpotentials in LSV measurements compared to both Co_3O_4@CC and Ni_xB@CC, likely due to the higher density of accessible active sites and improved electron transport pathways created by its multi-phase architecture. The slightly higher Tafel slope in Ni_xB/CoO-100@CC may indicate a shift in the rate-determining step or increased mechanistic complexity, consistent with recent work showing that Tafel slopes can reflect transitions in reaction pathways rather than intrinsic kinetics alone.[38]

ECSA estimation typically relies on double-layer capacitance (C_{dl}) measurements obtained from CVs in the non-faradaic region. However, C_{dl} measurements for transition metal oxides and hydroxides can be impacted by side reactions, including corrosion and specific adsorption, leading to potential overestimation of capacitance values.[39] Additionally, it was

 This journal is © The Royal Society of Chemistry 2026

Open Access Article. Published on 05 February 2026. Downloaded on 4/16/2026 1:51:50 AM. This article is licensed under a Creative Commons Attribution 3.0 Unported Licence.

observed that the Ni_xB/CoO@CC composites exhibited limited capacitive regions within the required voltage range, complicating the determination of C_{dl} using CV measurements. To address these challenges, the ECSA was estimated through electrochemical impedance spectroscopy (EIS) in the non-faradaic region (Fig. 3(d)) by fitting to a simple Randles cell model, yielding capacitance values which were further used to calculate both the absolute and relative ECSA values, as illustrated in Table S2. To calculate the absolute ECSA, the specific capacitance of 40 μF cm^{-2} (a typical value for atomically flat transition metal oxides in KOH) was compared with the recorded capacitance values. This approach yielded estimated ECSA values of 97.84 cm^2 mg^{-1} for Ni_xB/CoO-100@CC, 30.44 cm^2 mg^{-1} for Ni_xB@CC, and 59.60 cm^2 mg^{-1} for Co_3O_4@CC. Additionally, using the capacitance of the bare CC as a baseline reference, the relative ECSA ratios of 20.1, 6.25 and 12.24 for Ni_xB/CoO-100@CC, Co_3O_4@CC and Ni_xB@CC were obtained (Fig. 3(e)). This analysis indicates a substantial increase in electrochemically active sites in the mixed-phase composite Ni_xB/CoO-100@CC.

Further analysis of the charge-transfer properties was conducted using EIS (Fig. S6) under catalytic turnover conditions (1.6 V *vs.* RHE), and the corresponding equivalent circuit, fitted data and circuit parameters are summarised in Table S3. A low charge-transfer resistance of 1.53 ± 0.04 Ω was observed for Ni_xB/CoO-100@CC, with a similarly low value of 1.57 ± 0.06 Ω for Ni_xB@CC, while a slightly higher resistance of 4.47 ± 0.05 Ω was seen with Co_3O_4@CC, indicating that the Ni_xB enhances the conductivity of the composite. This low charge-transfer resistance and the structural characteristics of the Ni_xB/CoO-100@CC likely contribute to its enhanced OER performance. The increased ECSA of the composite suggests an increase in catalytic sites and activity. Meanwhile, the hierarchical 0D/2D structure provides a conducting, high-surface-area structural support that stabilises the Ni_xB particles, reducing agglomeration and thereby preserving site availability. Additionally, the presence of multiple redox-active species may enhance the adsorption of intermediates and catalytic turnover. The Ni_xB/CoO-100@CC also exhibits a low charge-transfer resistance due to the presence of Ni_xB, which enhances electron transport. Collectively, these factors contribute to the improved catalytic activity observed for the composite material.

Initial details regarding the stability of the Ni_xB/CoO-100@CC were obtained at a constant potential of 1.6 V *vs.* RHE. These data are presented in Fig. 3(f). It is apparent that a slight current decay occurs over the 24-h period, which may be attributed to the oxidative degradation of the CC substrate under prolonged anodic polarisation at this relatively high potential.[40] Subsequently, the LSV was recorded and compared to that of a freshly prepared electrocatalyst. These data are illustrated in the inset of Fig. 3(f). The LSV curves are comparable, showing only a slight reduction in OER activity after the 24-h stability test.

3.3 Electrochemical performance of Ni_xB/CoO-100 on NF

To validate the applicability of the Ni_xB/CoO catalyst on a practical electrode substrate, the optimised Ni_xB/CoO-100 catalyst was applied to a 1 × 1 cm^2, 0.1 mm thick piece of pressed NF and evaluated as an electrocatalyst for the OER. SEM analysis (Fig. 4(a)) reveals a uniform coating of the catalytic ink on the pressed NF. CV cycling (Fig. 4(b)) of the Ni_xB/CoO-100 composite on the NF substrate (Ni_xB/CoO-100@NF) shows a marked increase in current response compared to the bare NF electrode, indicating enhanced electrochemical activity and suggesting the deposited composite provides additional redox-active sites beyond the intrinsic contribution of the NF. Interestingly, on comparing these data to the corresponding study at CC, the high conductivity of the NF becomes apparent. The oxidation peak potential is centred at 0.52 V in Fig. 4(b), but at a higher potential of 0.57 V in Fig. 3(a). Likewise, there is a difference in the reduction peak potentials, which appear at 0.34 V for the NF and at 0.23 V for the CC substrate.

The stability of the Ni_xB/CoO-100@NF was studied over a 70-h period at a fixed potential of 1.6 V *vs.* RHE, and the corresponding current-time plot is shown in Fig. 4(c). After an initial slight decrease in the current over the first 10 h, it remains largely unchanged, confirming the retention of catalytic performance. Following the 70-h period, the electrode was polarised for a further 24 h at a higher current density of 50 mA cm^{-2}. The corresponding plot is shown in the inset of Fig. 4(c). Again, very good stability is seen for this additional 24-h period. After this 94-h long-term stability testing period, the LSV was measured and compared to a newly prepared electrocatalyst. The corresponding LSVs are presented in Fig. 4(d), indicating excellent OER activity. The two plots show minimal differences, with nearly identical onset potentials. At a high current density of 200 mA cm^{-2}, the overpotentials are 391 mV for the freshly prepared Ni_xB/CoO-100@NF compared to 419 mV following a 94-h stability study. The minimal degradation over this extended period supports the suitability of Ni_xB/CoO-100@NF catalyst for further development under more industrially relevant conditions. Indeed, the SEM observed after stabilisation, as shown in Fig. 4(e), clearly resembles the morphology presented in Fig. 4(a), with no evidence of any change in the surface morphology following stability.

It is evident from Fig. 4(d) that the NF exhibits OER activity, and this clearly contributes to the high OER activity of the Ni_xB/CoO-100 electrocatalyst. To establish this contribution, the OER performances of Ni_xB/CoO-100@NF, Ni_xB/CoO-100@CC, CC and NF were assessed using LSV studies. The corresponding LSV data are presented in Fig. S7. Here, it is clear that the Ni_xB/CoO-100 supported on the NF substrate has a higher OER activity, and this is associated with both the high conductivity of NF and its OER activity. However, the Ni_xB/CoO-100@NF clearly enhances the OER performance of the NF, and more particularly the CC.

Furthermore, the Ni_xB/CoO-100@NF compares very favourably with RuO_2/NF, achieving higher OER activity. Indeed, the Ni_xB/CoO-100@NF and RuO_2/NF have similar onset potentials at 317 and 313 mV, respectively, while the overpotentials at a much higher current density of 200 mA cm^{-2} are 483 mV for RuO_2/NF, but lower at 391 mV for Ni_xB/CoO-100@NF. Furthermore, the Ni_xB/CoO-100@NF performs well compared to other OER electrocatalysts, as highlighted in Table S4. Regarding the

Open Access Article. Published on 05 February 2026. Downloaded on 4/16/2026 1:51:50 AM.
This article is licensed under a Creative Commons Attribution 3.0 Unported Licence.

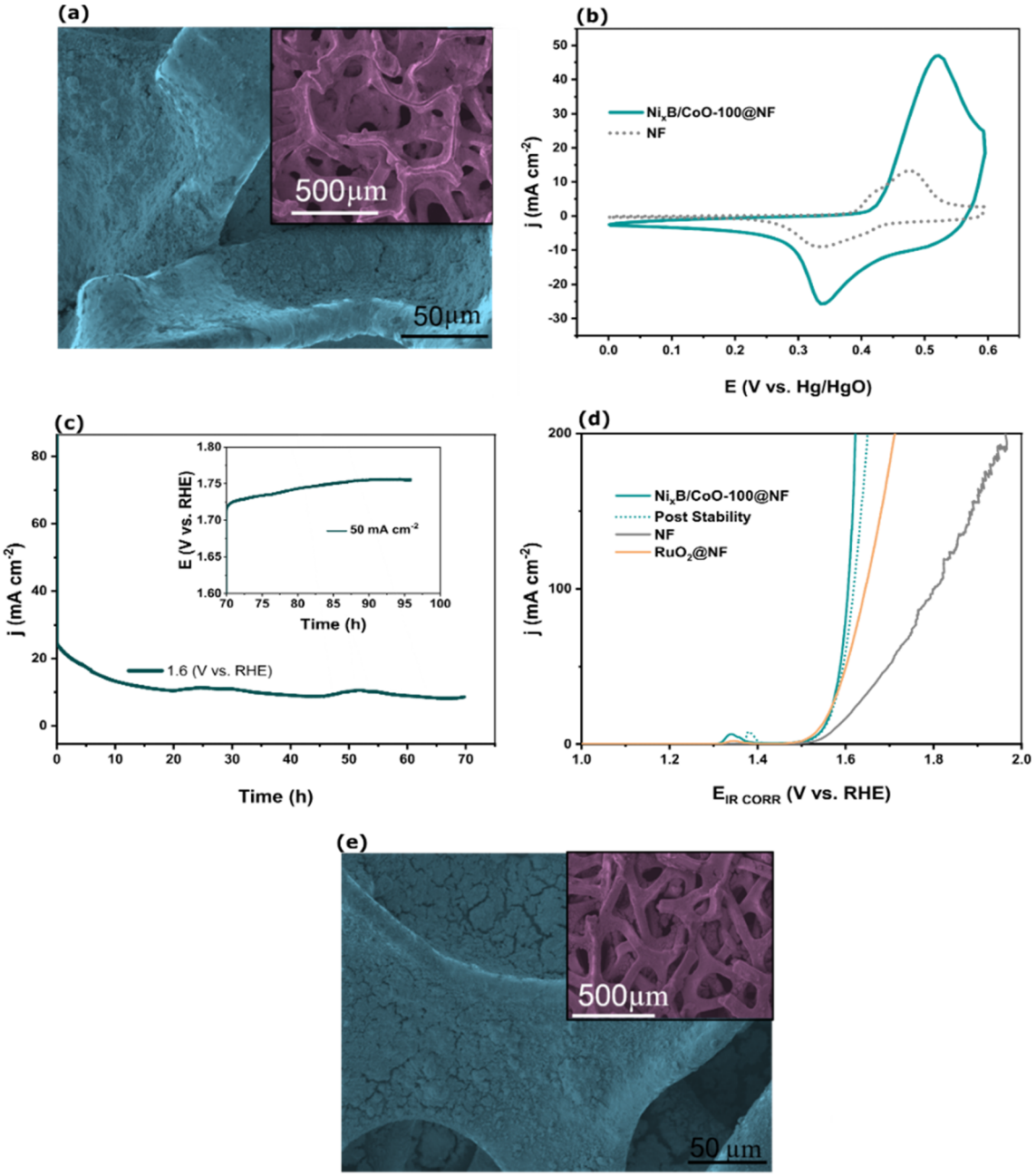

Fig. 4 (a) SEM characterisation of Ni$_x$B/CoO-100@NF as prepared, (b) CV cycling at 50 mV s^{-1} in 1.0 M KOH (c) Chronoamperometric and (inset) chronopotentiometric stability testing in 1.0 M KOH. (d) LSV at 2 mV s^{-1} before and following stability testing, and (e) SEM characterisation of Ni$_x$B/CoO-100@NF following 94 h of continuous operation.

cobalt-based electrocatalysts, such as $CoMoO_4$,[41] with an overpotential of 366 mV at 10 mA cm^{-2} (η_{10}), and stability over 80 h, the Co_2CrO_4/RuO_2,[42] with stability over 60 h and $\eta_{10} = 209$ mV, and Co_3Fe_7/Fe_3O_4,[43] with $\eta_{10} = 279$ mV and stability for 12 h, the Ni$_x$B/CoO-100@NF performs well, achieving an η_{10} of 316 with stability over 94 h. However, the benefit of the Ni$_x$B/CoO-100@NF system lies in its high OER currents at relatively low overpotentials. Many of the electrocatalysts in Table S4 require overpotentials greater than 400 mV to achieve 100 mA cm^{-2}. In contrast, the overpotential of Ni$_x$B/CoO-100@NF at 100 mA cm^{-2} is only 391 mV. Furthermore, the Ni$_x$B/CoO-100@NF compares well with the widely reported layered double hydroxides, including doped FeNi-LDH[44] (Table S4).

3.4 Post-stability characterisation of Ni$_x$B/CoO-100 on NF

To investigate surface reconstruction, high-resolution XPS was conducted on the Ni$_x$B/CoO-100@NF composite after 70 h of continuous operation at 1.6 V *vs.* RHE in 1.0 M KOH (Fig. 5(a–c)). These spectra were compared with those in Fig. 2(c–f). In the Ni 2p region, a clear transformation from metallic Ni^0/Ni–B (851.9 eV) to oxidised species is observed. Following prolonged

 This journal is © The Royal Society of Chemistry 2026

Open Access Article. Published on 05 February 2026. Downloaded on 4/16/2026 1:51:50 AM.
This article is licensed under a Creative Commons Attribution 3.0 Unported Licence.

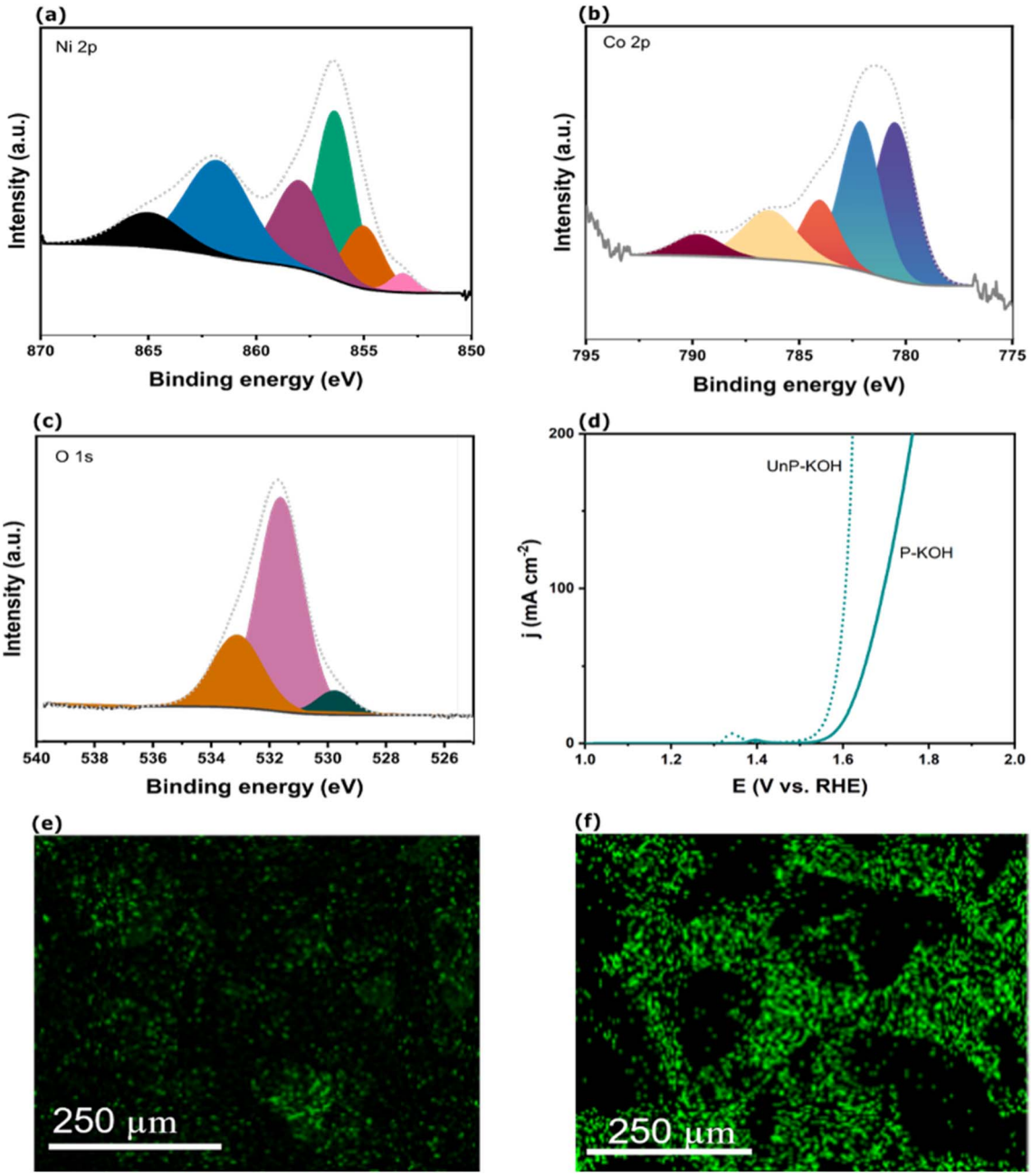

Fig. 5 XPS analysis of (a) Ni 2p, (b) Co 2p and (c) O 1s regions of Ni_xB/CoO-100@CC following 70 h of continuous operation at 1.6 V Vs RHE in 1.0 M KOH, (d) LSV of Ni_xB/CoO-100@NF at 2 mV s^{-1} in purified and un-purified 1.0 M KOH and (e) EDX analysis showing Fe incorporation following activation and (f) following 70 h of continuous operation at 1.6 V *vs.* RHE in 1.0 M KOH.

exposure to OER conditions, the Ni^0 disappears entirely, replaced by dominant features at 853.2 eV (Ni–O), 855.0 eV ($Ni(OH)_2$), and a new feature at 856.3 eV attributed to NiOOH/Ni^{3+}, consistent with progressive oxidation reported for nickel boride surfaces undergoing electrochemical activation and reconstruction.[13] This progressive oxidation indicates the *in situ* formation of a catalytically active nickel (oxy)hydroxide phase during OER. Similarly, the Co 2p spectra support oxidation from the initial mixed Co_3O_4 to higher valent species. Following the long-term stability, prominent peaks at 782.1 and 784.0 eV are assigned to $Co(OH)_2$ and CoOOH, respectively, consistent with the oxidation of the cobalt support under OER conditions.[45] The O 1 s spectra support these findings. Initially, peaks at 531.0 and 529.1 eV correspond to hydroxide ($Ni(OH)_2$/$Co(OH)_2$) and oxide (Ni–O/Co–O) species, respectively. After extended testing, the hydroxide signal shifts to 531.6 eV, suggesting further oxidation and the formation of oxyhydroxide phases, consistent with the growth of NiOOH and CoOOH. Notably, B 1s signals present after activation, specifically B–O (191.9 eV) and B_2O_3 (193.0 eV) are no longer detectable following extended OER testing. This suggests substantial boron loss from the surface, likely as soluble borate species under alkaline conditions. This

Open Access Article. Published on 05 February 2026. Downloaded on 4/16/2026 1:51:50 AM.
This article is licensed under a Creative Commons Attribution 3.0 Unported Licence.

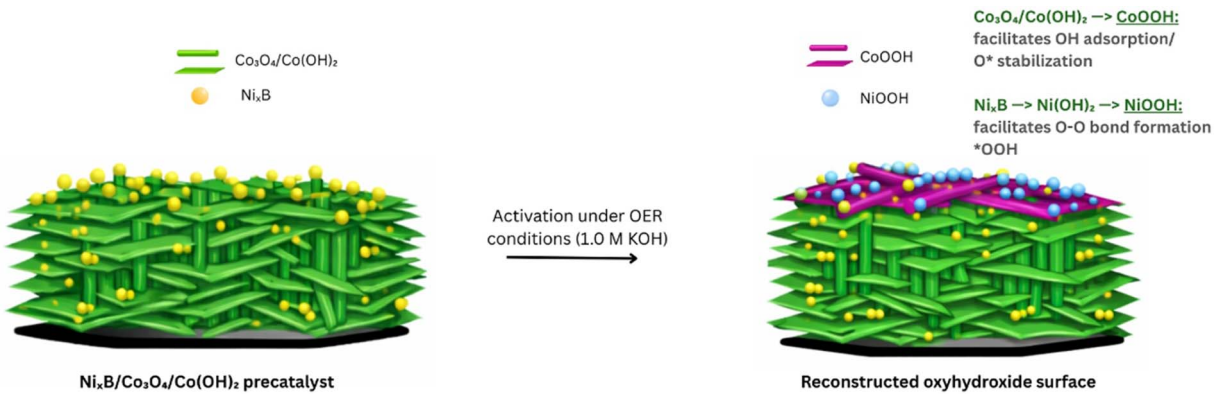

Scheme 2 Schematic representation of the Ni_xB/CoO-100 and its surface reconstruction to give oxyhydroxide CoOOH and NiOOH species.

behaviour is consistent with reports for TM boride electrocatalysts, where surface boron is oxidised to soluble $B(OH)_4^-$ at OER-relevant potentials, leaving behind a boron-deficient (oxy) hydroxide surface.[46] While some studies have observed retained oxidised boron (*e.g.*, BO_2^-) influencing OER-active sites, the complete disappearance of B species in our system supports a model where Ni_xB serves as a pre-catalyst that transforms into a NiOOH/CoOOH-rich surface during OER. This aligns with the broader classification of TM borides as pre-catalysts rather than persistent active phases.[7,47] In our system, the emergence of Ni^{3+} and Co^{3+} species alongside the disappearance of B signals supports a similar pre-catalytic mechanism, wherein the Ni_xB/CoO interface reconstructs into a mixed (oxy)hydroxide-rich surface.[48,49] This supports the role of the boride phase as enhancing catalytic activity through *in situ* transformation, rather than *via* direct involvement of B-containing species in the OER process. On the basis of this reconstructed oxyhydroxide-rich surface, the OER mechanism is assumed to proceed *via* the adsorbate evolution mechanism (AEM) described in eqn (5)–(8) and shown schematically in Scheme 2.

$$H_2O + * \rightarrow OH^* + e^- + H^+ \quad (5)$$

$$OH^* \rightarrow O^* + e^- + H^+ \quad (6)$$

$$O^* + H_2O \rightarrow HOO^* + e^- + H^+ \quad (7)$$

$$HOO^* \rightarrow * + O_2 + e^- + H^+ \quad (8)$$

The first step involves OH* adsorption, followed by deprotonation of the hydroxyl species, O–O bond formation *via* OOH* and subsequent O_2 release. In this system, surface CoOOH is expected to favour OH* adsorption and stabilisation of O* intermediates, while NiOOH sites facilitate O–O bond formation, providing a synergistic environment for the AEM which is consistent with the enhanced OER activity observed (Scheme 2).[50]

Consistent with previous studies, EDX (Fig. 5(e)) elemental mapping revealed the early-stage post-activation incorporation of Fe into the catalyst surface, and this appears to increase with prolonged electrochemical operation, as evidenced by post-stability EDX analysis (Fig. 5(f)). This incorporation, likely into the $Ni(OH)_2$ layer, is well documented to enhance OER activity in alkaline media.[51] The purification method developed by Marquez *et al.* was followed.[52] As shown in Fig. 5(d), the performance was improved when using unpurified KOH (UnP-KOH) compared to the purified (P-KOH) electrolyte, further suggesting that trace Fe in the electrolyte contributes to the formation of a more active FeNi(OOH) layer at the surface of the Ni_xB/CoO.

4. Conclusion

In this study, we demonstrate the development of a mixed-phase Ni_xB/CoO-100@NF pre-electrocatalyst for OER in alkaline media. The catalyst, fabricated *via* a simple chemical reduction method, integrates amorphous nickel boride particles with cobalt oxide rods and hydroxide sheets to yield a highly active and stable composite. Among the series, the Ni_xB/CoO-100 composite exhibited the best performance, achieving an overpotential of just 370 mV at 100 mA cm^{-2}. Post-OER XPS analysis revealed a dynamic reconstruction mechanism wherein the initial boride and oxide phases transform into catalytically active Ni^{3+}/Co^{3+} (oxy)hydroxide species. The disappearance of B 1s signals and the formation of NiOOH/CoOOH suggest a pre-catalyst behaviour, with the boride acting as a sacrificial precursor. Additional evidence of Fe incorporation during activation further highlights the dynamic nature of the catalytic surface and its role in boosting OER activity.

Finally, the successful translation of the optimised catalyst coated onto an NF substrate underscores its potential for application in practical alkaline electrolysis systems. The stability of the material under prolonged electrolysis positions it as a promising candidate for scalable, cost-effective water splitting technologies.

Conflicts of interest

There are no conflicts to declare.

 This journal is © The Royal Society of Chemistry 2026

Open Access Article. Published on 05 February 2026. Downloaded on 4/16/2026 1:51:50 AM. This article is licensed under a Creative Commons Attribution 3.0 Unported Licence.

Data availability

Data will be made available on request.

Supplementary information (SI) is available. See DOI: https://doi.org/10.1039/d5se01506e.

Acknowledgements

This publication has emanated from research conducted with the financial support of Research Ireland under grant numbers IRC/GOIPG/2022/1605 and SFI/20/FFP-P/8793, the Sustainable Energy Authority of Ireland, grant number SEAI/22/RDD/841, and the EU Horizon 2020 program under the Marie Skłodowska-Curie grant no. 101106064.

References

1 M. Chen and J. Guan, *Adv. Funct. Mater.*, 2025, **35**(30), 2423552, DOI: 10.1002/adfm.202423552.
2 M. Yagi and M. Kaneko, *Chem. Rev.*, 2001, **101**(1), 21, DOI: 10.1021/cr980108l.
3 X. Long, J. Li, S. Xiao, K. Yan, Z. Wang, H. Chen and S. Yang, *Angew. Chem.*, 2014, **126**(29), 7584, DOI: 10.1002/ange.201402822.
4 M. R. Gao, Y. F. Xu, J. Jiang, Y. R. Zheng and S. H. Yu, *J. Am. Chem. Soc.*, 2012, **134**(6), 2930, DOI: 10.1021/ja211526y.
5 O. Mabayoje, A. Shoola, B. R. Wygant and C. B. Mullins, *ACS Energy Lett.*, 2016, **1**(1), 195, DOI: 10.1021/acsenergylett.6b00084.
6 Y. Zhu, H. C. Chen, C. S. Hsu, T. S. Lin, C. J. Chang, S. C. Chang, L. D. Tsai and H. M. Chen, *ACS Energy Lett.*, 2019, **4**(4), 987, DOI: 10.1021/acsenergylett.9b00382.
7 B. R. Wygant, K. Kawashima and C. B. Mullins, *ACS Energy Lett.*, 2018, **3**(12), 2956, DOI: 10.1021/acsenergylett.8b01774.
8 W. Chen, H. Wang, Y. Li, Y. Liu, J. Sun, S. Lee, J. S. Lee and Y. Cui, *ACS Cent. Sci.*, 2015, **1**(5), 244, DOI: 10.1021/acscentsci.5b00227.
9 W. Chen, Y. Liu, Y. Li, J. Sun, Y. Qiu, C. Liu, G. Zhou and Y. Cui, *Nano Lett.*, 2016, **16**(12), 7588, DOI: 10.1021/acs.nanolett.6b03458.
10 J. Liu and D. Xue, *Adv. Mater.*, 2008, **20**(13), 2622, DOI: 10.1002/adma.200800208.
11 F. Song, T. Zhang, Y. Qian, J. Shaw, S. Chen, G. Chen, Y. Sun and Y. Rao, *Mater. Today Energy*, 2021, **22**, 100846, DOI: 10.1016/j.mtener.2021.100846.
12 X. Chen, Z. Yu, L. Wei, Z. Zhou, S. Zhai, J. Chen, Y. Wang, Q. Huang, H. E. Karahan, X. Liao and Y. Chen, *J. Mater. Chem. A Mater.*, 2019, **7**(2), 764, DOI: 10.1039/c8ta09130g.
13 J. Masa, I. Sinev, H. Mistry, E. Ventosa, M. de la Mata, J. Arbiol, M. Muhler, B. Roldan Cuenya and W. Schuhmann, *Adv. Energy Mater.*, 2017, **7**(17), 1700381, DOI: 10.1002/aenm.201700381.
14 R. Sukanya, R. Karthik, M. Hasan, C. Breslin and J. J. Shim, *Chem. Eng. J.*, 2023, **473**, 145487, DOI: 10.1016/j.cej.2023.145487.
15 Y. Du, X. He, C. Yan, Q. Hu, J. Zhang and F. Yang, *J. Mater. Chem. A Mater.*, 2025, **13**(11), 7962, DOI: 10.1039/d4ta08295h.
16 Y. Kang, B. Jiang, V. Malgras, Y. Guo, O. Cretu, K. Kimoto, A. Ashok, Z. Wan, H. Li, Y. Sugahara, Y. Yamauchi and T. Asahi, *Small Methods*, 2021, **5**(10), 2100679, DOI: 10.1002/smtd.202100679.
17 X. Cao, X. Wang, L. Cui, D. Jiang, Y. Zheng and J. Liu, *Chem. Eng. J.*, 2017, **327**, 1085, DOI: 10.1016/j.cej.2017.07.010.
18 J. L. Hauser, G. Amberchan, M. Tso, R. Manley, K. Bustillo, J. Cooper, J. H. Golden, B. Singaram and S. R. J. Oliver, *ACS Appl. Nano Mater.*, 2019, **2**(3), 1472, DOI: 10.1021/acsanm.8b02351.
19 F. Yang, X. J. Ma, J. L. Yang, J. H. Liu, B. Chen, X. Y. Liu, K. Yang and W. Bin Zhang, *Appl. Clay Sci.*, 2024, **251**, 107305, DOI: 10.1016/j.clay.2024.107305.
20 F. Lyu, Q. Wang, S. M. Choi and Y. Yin, *Small*, 2019, **15**, 1804201, DOI: 10.1002/smll.201804201.
21 Z. Liang, D. Shen, L. Wang and H. Fu, *Nano Res.*, 2024, **17**(4), 2234, DOI: 10.1007/s12274-023-6219-4.
22 Z. Liang, D. Shen, L. Wang and H. Fu, *Small*, 2021, **17**, 2100129, DOI: 10.1002/smll.202100129.
23 S. Möller, S. Barwe, J. Masa, D. Wintrich, S. Seisel, H. Baltruschat and W. Schuhmann, *Angew. Chem., Int. Ed.*, 2020, **59**(4), 1585, DOI: 10.1002/anie.201909475.
24 W. Zheng, M. Liu and L. Y. S. Lee, *ACS Energy Lett.*, 2020, **5**(10), 3260, DOI: 10.1021/acsenergylett.0c01958.
25 W. Li, S. Wang, M. Wu, X. Wang, Y. Long and X. Lou, *New J. Chem.*, 2017, **41**(15), 7302, DOI: 10.1039/c7nj00222j.
26 A. K. Dimble, N. D. Bagul, P. C. Walimbe, P. S. Kulkarni and S. D. Kulkarni, *Langmuir*, 2024, **40**(35), 18631, DOI: 10.1021/acs.langmuir.4c02149.
27 G. Rathika, V. Suba, D. S. Lakshmi and R. Rani, *J. Inorg. Organomet. Polym. Mater.*, 2022, **32**(8), 3153, DOI: 10.1007/s10904-022-02348-3.
28 F. Zhang, C. Yuan, X. Lu, L. Zhang, Q. Che and X. Zhang, *J. Power Sources*, 2012, **203**, 250, DOI: 10.1016/j.jpowsour.2011.12.001.
29 H. B. Li, M. H. Yu, X. H. Lu, P. Liu, Y. Liang, J. Xiao, Y. X. Tong and G. W. Yang, *ACS Appl. Mater. Interfaces*, 2014, **6**(2), 745, DOI: 10.1021/am404769z.
30 T. J. Chuang, C. R. Brundle and D. W. Rice, *Surf. Sci.*, 1976, **59**(2), 413, DOI: 10.1016/0039-6028(76)90026-1.
31 S. Gupta, N. Patel, A. Miotello and D. C. Kothari, *J. Power Sources*, 2015, **279**, 620, DOI: 10.1016/j.jpowsour.2015.01.009.
32 J. Wu, M. Hou, Z. Chen, W. Hao, X. Pan, H. Yang, W. Cen, Y. Liu, H. Huang, P. W. Menezes and Z. Kang, *Adv. Mater.*, 2022, **34**(32), 2202995, DOI: 10.1002/adma.202202995.
33 W. Wang, Y. Zhong, X. Zhang, S. Zhu, Y. Tao, Y. Zhang, H. Zhu, Y. Zhang, X. Wu and G. Hong, *J. Colloid Interface Sci.*, 2021, **582**, 803, DOI: 10.1016/j.jcis.2020.08.095.
34 C. Qiu, F. Maroun, M. Bouvier, I. Pacheco, P. Allongue, T. Wiegmann, C. Hendric Scharf, V. de Manuel-Gonzalez, F. Reikowski, J. Stettner, J. Stettner and O. M. Magnussen, *ChemCatChem*, 2024, **16**(23), e202400988, DOI: 10.1002/cctc.202400988.

Open Access Article. Published on 05 February 2026. Downloaded on 4/16/2026 1:51:50 AM.
This article is licensed under a Creative Commons Attribution 3.0 Unported Licence.

35 J. T. Mefford, A. R. Akbashev, M. Kang, C. L. Bentley, W. E. Gent, H. D. Deng, D. H. Alsem, Y.-S. Yu, N. J. Salmon, D. A. Shapiro, P. R. Unwin and W. C. Chueh, *Nature*, 2021, **593**(7857), 67, DOI: 10.1038/s41586-021-03454-x.

36 S. Anantharaj, S. Noda, M. Driess and P. W. Menezes, *ACS Energy Lett.*, 2021, **6**, 4–1607, DOI: 10.1021/acsenergylett.1c00608.

37 A. Sengeni and S. Noda, *Mater. Today Energy*, 2022, **29**, 101123, DOI: 10.1016/j.mtener.2022.101123.

38 O. van der Heijden, S. Park, R. E. Vos, J. J. J. Eggebeen and M. T. M. Koper, *ACS Energy Lett.*, 2024, **9**(4), 1871, DOI: 10.1021/acsenergylett.4c00266.

39 C. Wei, S. Sun, D. Mandler, X. Wang, S. Z. Qiao and Z. J. Xu, *Chem. Soc. Reviews.*, 2019, (48), 2518, DOI: 10.1039/c8cs00848e.

40 T. Wu, M. Han, X. Zhu, G. Wang, H. Zhang and H. Zhao, *Chem. Commun.*, 2019, **55**(16), 2344, DOI: 10.1039/c9cc00398c.

41 X. Zhong, Y. Chen, T. Gan, Y. Huang, J. Li and S. Zhang, *Nano Res.*, 2025, **18**(3), 94907204, DOI: 10.26599/NR.2025.94907204.

42 M. Qi, X. Zheng, H. Tong, Y. Liu, D. Li, Z. Yan and D. Jiang, *J. Colloid Interface Sci.*, 2025, **677**, 548, DOI: 10.1016/j.jcis.2024.07.260.

43 R. Barath, S. Vadivel, S. Sarmila, P. Sujita, N. Murugan and Y. A. Kim, *Mater. Lett.*, 2025, **399**, 139056, DOI: 10.1016/j.matlet.2025.139056.

44 Y. Lv, X. Deng, J. Ding and Y. Zhou, *Sci. Rep.*, 2024, **14**, 902, DOI: 10.1038/s41598-023-50361-4.

45 T. Tran-Phu, R. Daiyan, J. Leverett, Z. Fusco, A. Tadich, I. Di Bernardo, A. Kiy, T. N. Truong, Q. Zhang, H. Chen, P. Kluth, R. Amal and A. Tricoli, *Chem. Eng. J.*, 2022, **429**, 132180, DOI: 10.1016/j.cej.2021.132180.

46 A. M. Zieschang, J. D. Bocarsly, J. Schuch, C. V. Reichel, B. Kaiser, W. Jaegermann, R. Seshadri and B. Albert, *Inorg. Chem.*, 2019, **58**(24), 16609, DOI: 10.1021/acs.inorgchem.9b02617.

47 K. Kawashima, R. A. Márquez, L. A. Smith, R. R. Vaidyula, O. A. Carrasco-Jaim, Z. Wang, Y. J. Son, C. L. Cao and C. B. Mullins, *Chem. Rev.*, 2023, **123**, 23–12795, DOI: 10.1021/acs.chemrev.3c00005.

48 S. Gul, J. W. D. Ng, R. Alonso-Mori, J. Kern, D. Sokaras, E. Anzenberg, B. Lassalle-Kaiser, Y. Gorlin, T.-C. Weng, P. H. Zwart, J. Z. Zhang, U. Bergmann, V. K. Yachandra, T. F. Jaramillo and J. Yano, *Phys. Chem. Chem. Phys.*, 2015, **17**(14), 8901, DOI: 10.1039/c5cp01023c.

49 R.-Y. Fan, J.-Y. Xie, N. Yu, Y.-M. Chai and B. Dong, *Int. J. Hydrogen Energy*, 2022, **47**(19), 10547, DOI: 10.1016/j.ijhydene.2021.12.239.

50 Y. Zhang, C. Han, J. Gao, L. Pan, J. Wu, X. Zhu and J.-J. Zou, *ACS Catal.*, 2021, **11**(20), 12485, DOI: 10.1021/acscatal.1c03260.

51 S. Anantharaj, S. Kundu and S. Noda, *Nano Energy*, 2021, **80**, 105514, DOI: 10.1016/j.nanoen.2020.105514.

52 R. A. Márquez, K. Kawashima, Y. J. Son, G. Castelino, N. Miller, L. A. Smith, C. E. Chukwuneke and C. B. Mullins, *ACS Energy Lett.*, 2023, **8**(2), 1141, DOI: 10.1021/acsenergylett.2c02847.

This journal is © The Royal Society of Chemistry 2026